Lab on a Chip

PAPER

View Article Online
View Journal | View Issue

Cite this: *Lab Chip*, 2025, **25**, 5524

A novel holder and microfluidic system for spatially controlled hypoxia induction, mechanical stimulation and cardiac regeneration research

Kołodziejek Dominik, [a] Szlachetka Aleksandra, [a] Iwoń-Szczawińska Zuzanna,[ac] Drozd Marcin, [c] Wojasiński Michał [b] and Jastrzębska Elżbieta *[ac]

Received 9th May 2025,
Accepted 9th September 2025

DOI: 10.1039/d5lc00460h

rsc.li/loc

Over the years, cardiovascular diseases have remained a leading cause of mortality worldwide, necessitating advanced experimental models to mimic the natural environment of the heart as closely as possible. New microfluidic heart models would enable precise modelling of the healthy heart as well as pathological mechanisms occurring during cardiac ischemia and testing new therapies would become more accessible than it is currently. In this study, we developed a two layer holder for creating hypoxic conditions in a dedicated microfluidic system for modelling cardiac infarction. By integrating the holder with a microsystem utilizing nanofibrous mats with iron(II, III) oxide (Fe_3O_4) magnetic nanoparticles we were able to create a tool for using (potentially patient specific) induced pluripotent stem cell-derived cardiomyocytes (iPSC-CMs) in cardiac research. In the microsystem we induced hypoxia and conducted preliminary observations of cardiac regeneration using induced pluripotent stem cells (iPSCs). We found that iPSCs express cTnT when co-cultured with hypoxia-damaged iPSC-CMs indicating that the holder with an integrated microsystem can be used for hypoxia and cardiac regeneration studies.

Introduction

Cardiovascular diseases (CVDs) are currently one of the most common and serious conditions among people around the world. An important characteristic of CVDs is their high heterogeneity in both risk factors and clinical symptoms, making diagnosis and treatment difficult. CVDs account for approximately 30% of global mortality, which means they are more lethal than cancers. Classical diagnosis tools include electrocardiography (ECG), echocardiography, computer tomography (CT), magnetic resonance imaging (MRI), and angiography. Precise diagnosis is important not only for early detection of illnesses but also for monitoring patients and evaluating the effectiveness of treatments. Research has allowed for improved diagnostic methods and therapeutics and has broadened our knowledge about risk factors and disease mechanisms at the cellular level. In recent years, we have seen opportunities for using non-coding RNAs in diagnosing and treating CVD,[1] using artificial intelligence and machine learning to analyze images obtained from imaging-based diagnostic techniques,[2] and using nanoparticles to treat CVD.[3] However, current *in vitro* models used in CVD studies do not mimic the microenvironment of human heart tissue in a precise manner, since most commercially used models rely on two-dimensional (2D) cell cultures or animal tissues. Easy-to-use and advanced cellular models would allow for improved studies of new diagnostic and treatment tools, as they closely replicate the *in vivo* conditions of the heart compared to currently used models. Moreover, there is a growing demand to limit the usage of animals in pharmaceutical research, and accurate *in vitro* models could also serve as a solution. A promising aspect of disease research in this context has become organ-on-a-chip technology.

Organ-on-a-chip systems are small devices, typically made from elastomers and/or glass, containing microstructures (*e.g.*, microchannels, microchambers) that allow for the appropriate geometry for cell culture and *in vitro* modelling of human organs.[4] Due to their small size, they require smaller amounts of culture media and reagents than traditional cell culture, while utilizing unique characteristics of the microscale (such as laminar flow or effective diffusion).[5,6] This allows for replication of the tissue microenvironment that is more accurate to *in vivo* conditions compared to macroscale cell cultures.[7] Advantages of a microscale cell culture include reduced reagent usage and the possibility of closely recreating the microenvironment of human organs.[8–10]

[a] *Chair of Medical Biotechnology, Faculty of Chemistry, Warsaw University of Technology, Poland. E-mail: elzbieta.jastrzebska@pw.edu.pl*
[b] *Department of Biotechnology and Bioprocess Engineering, Faculty of Chemical and Process Engineering, Warsaw University of Technology, Poland*
[c] *Center for Advanced Materials and Technologies, Warsaw University of Technology, Poland*

Due to their versatility, organ-on-a-chip devices can be used to model specific organs, such as the lungs, liver, bones, brain, or, as in this study, the heart.[11–15] As the heart is an electrophysiological pump powered by the rhythmic contractions of cardiomyocytes, heart-on-a-chip models focus mainly on creating an *in vitro* model where cardiomyocytes are encouraged to express their native characteristics – elongated shape, electrophysiological activity, and the ability to contract spontaneously and in a uniform way.[7] Since there does not exist an established adult cardiomyocyte cell line, research focuses mostly on primary human cardiomyocytes (HCM), primary rat cardiomyocytes, rat cardiac myoblast cells (H9C2), or stem cells differentiated into cardiomyocytes (human induced pluripotent stem cell-derived cardiomyocytes, iPSC-CMs).[16–19] For years, the most common cell line used as a human heart model was the H9C2 cell line, but since it is a myoblast, not a myocyte, cell line, and it is rat-derived, there was a significant flaw in those models. Recently, iPSC-CMs have gained popularity in cardiac research since they are the only non-primary human cardiomyocyte cell line and are obtained through iPSC differentiation with established protocols.[20] In future research, iPSCs will give the potential for personalized medicine and research models produced directly from a sample taken from a patient. An important flaw of both H9C2 and iPSC-CMs is that they are more similar to embryonic cardiomyocytes rather than adult ones, and they do not have all of the previously mentioned characteristics.[21,22] Therefore, engineering solutions that encourage cardiomyocyte maturation play a crucial role in heart-on-a-chip devices.

An important element of promoting cardiomyocyte maturation is their stimulation. The stimuli can have various origins. For example, the laminar flow in the microsystem can act as stimulation itself, as it causes shear stress on the cell membranes and, in moderate conditions, encourages growth parallel to the direction of the flow. It has been shown that cardiomyocytes growing in a microfluidic device with flow conditions exhibit more mature characteristics than cells growing on a 6-well plate.[23] Moreover, the efficiency of flow stimulation highly depends on the shape of the microchamber, as the shape influences the geometry of the laminar flow. In our team's previous work, we showed that a rectangle is the optimal microchamber shape to encourage cardiac cell maturation.[24] In addition to flow, mechanical force can also be applied to the cell culture by stretching the surface on which the cells grow. In this solution, a highly elastic growth surface is usually used, and a stretching force is applied continuously or with relaxation periods on a single or multiple axes.[25,26] Electrodes are integrated into the culture in electrically simulated devices, and cells are treated with electrical impulses.[27] Electrical stimulation affects protein or gene levels and is highly associated with regulating the rhythm of cell stretching, so their spontaneous beating pattern is uniform throughout the whole culture.[28]

Many heart-on-a-chip devices include a 3D structural element for the cells to grow on and encourage maturation. This can be done by introducing a hydrogel or a scaffold material into the culture chamber prior to cell culture. Several works use gelatin, gelatin methacryloyl (GelMA), or other protein hydrogel solutions.[23,28,29] Polymer (and biopolymer) scaffolds can be created in a way to achieve the desired shape or pattern of the model.[30,31] Nanofibrous elements are rarely used in heart-on-a-chip systems; however, like polymer scaffolds, they offer possibilities of modification and specific use. For example, Lee *et al.* created polymer nanofibers modified with diazonium salts, which released nitrogen oxide into the microenvironment.[32] In our team's previous work, we demonstrated the potential use of polyurethane (PU) nanofibrous mats with regard to cardiomyocyte maturation.[33] The mats promoted the longitudinal shape of the cardiomyocytes and aided their maturation, creating a 3D healthy heart model. In this work, we decided to expand the capabilities of the model by replicating disease conditions – hypoxia.

Apart from achieving the maturity of cardiomyocytes in *in vitro* cultures, microfluidic models should also be able to recreate disease conditions, such as hypoxia. Studying cellular and molecular responses, such as metabolic shifts, that happen in cardiomyocytes under hypoxic conditions, can serve as a tool for understanding the pathogenesis of these diseases and uncovering new potential therapeutic targets. Low oxygen conditions can be induced in cellular models in various ways.

In macroscopic hypoxia research, cell culture vessels are usually placed in an incubator with a desired oxygen concentration.[34,35] This method can also be used for microscale cell cultures; however, due to the scale difference, there are problems with uneven distribution of oxygen concentrations and inefficient gas exchange. A straightforward translation of a commercial incubator to the microscale is to minimize the incubator itself by creating a small chamber with a nitrogen supply and placing a microsystem inside.[36] However, microsystems can be engineered to offer other, more specific solutions. The main way to generate hypoxia in a microfluidic cell culture is by diffusion, which reduces the oxygen concentration in the culture chamber. This is done mainly by designing additional channels around the chamber and introducing either oxygen scavenging reagents or nitrogen there. Oxygen scavenging reagents include sodium sulfite (with cobalt salt as a catalyst).[37–39] A different approach is to introduce nitrogen (or nitrogen/air or nitrogen/oxygen mixtures) to achieve specific oxygen concentrations.[40,41] Gas channels also allow for achieving oxygen gradients, which can be useful in studying tumor biology.[42]

To overcome the inadequacies of currently existing heart models and to allow for on-chip control cultures, we designed a microfluidic system with integrated polyurethane nanofibrous mats with magnetic nanoparticles and a dedicated holder to study the effects of hypoxia on a heart model (Fig. 1). The custom holder allowed for spatial control of oxygen concentrations, where two zones – a hypoxia zone and a normoxia zone are created. The aim of this research was to design a setup to study hypoxia in a heart model obtained in a novel heart-on-a-chip device. The device is intended to model

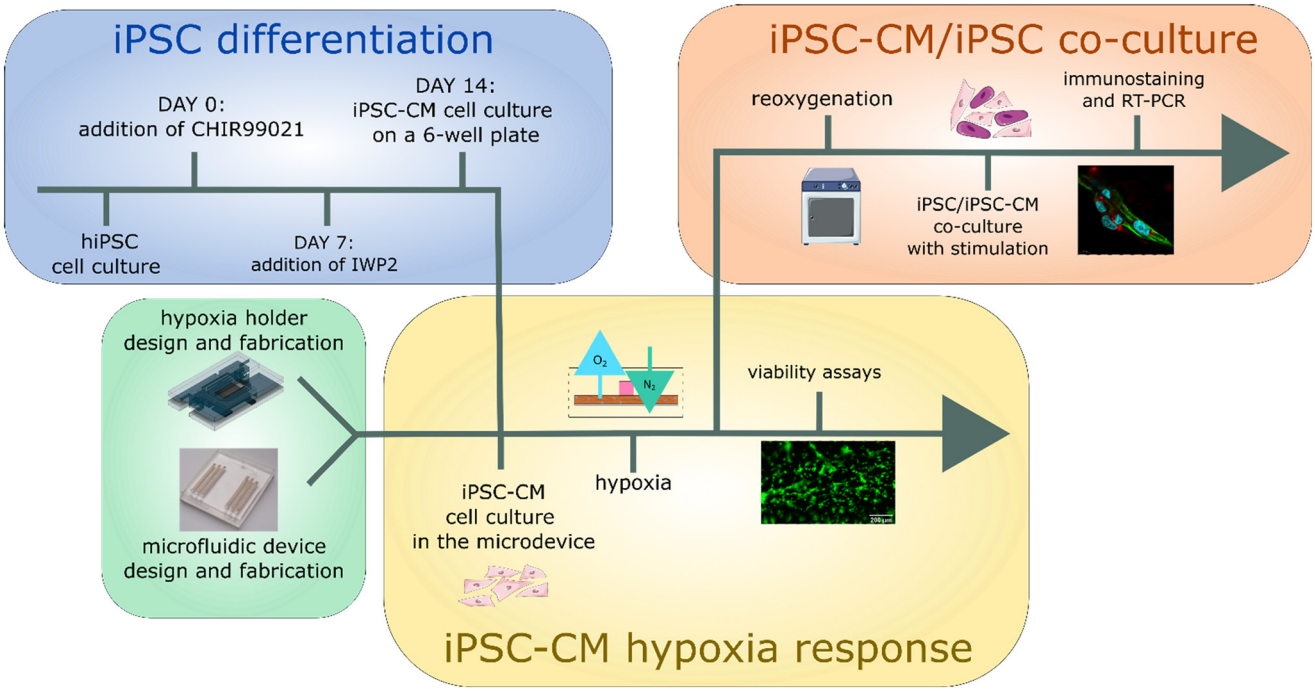

Fig. 1 Workflow diagram of the presented study. In this study we designed and created a heart-on-a-chip system and holder to recreate hypoxic conditions in cardiomyocyte cell culture and study cardiac regeneration. Firstly, an iPSC-CM cell culture in heart-on-a-chip system was exposed to hypoxic conditions for 6 h to mimic ischemic conditions in the heart and metabolic assays were conducted. Later, the culture was reoxygenated, as happens *in vivo* during post-ischemic reperfusion, and iPSCs were added to study stem cell cardiac muscle regeneration.

acute myocardial infarction (heart attack), replicating the sudden oxygen deprivation that occurs during this ischemic event. Additionally, we conducted cellular research and assessed its effect on cardiomyocyte function and maturation. This platform could provide valuable insights into cardiac ischemia and aid in the development of new therapeutic strategies.

Experimental

Materials and methods

Design and simulations. The microfluidic device and the mold were designed in Autodesk Fusion360. The device consists of one inlet (1.5 mm in diameter), 6 channels (0.5 × 0.5 mm), and 6 rectangular chambers (3 × 35 mm) with integrated nanofibrous mats (Fig. 2A–E). Three of the chambers are subjected to hypoxic conditions, and three remain in normoxia, therefore creating a 'hypoxia zone' and 'normoxia zone'. Additionally, the resulting oxygen levels should be even throughout the zones. The considered distances, 9, 13.5, 18, 22.5, and 27 mm, are all based on the distance between wells in a 384-well plate, to make the microsystem compatible with a plate reader. In the final microsystem, the zones are separated by a gap of 22.5 mm, which was chosen as the optimal distance after oxygen level simulations in Ansys (Fig. 2F). There are 6 outlets, one from each chamber. The rectangular shape of the chambers was chosen to encourage cardiomyocyte maturation as discussed in previous publications.[33] Total device measurements are 52 mm × 57 mm × 8 mm.

Numerical simulations. Numerical modelling of the oxygen gradient inside the microsystem was performed in ANSYS 2024 R3. Static conditions were assumed: no medium perfusion and no cellular uptake of oxygen. Transport therefore occurred exclusively by molecular diffusion through the poly(dimethylsiloxane) (PDMS) walls and subsequently within the culture chambers. The steady-state distribution of dissolved oxygen, C [mol m^{-3}], was described by the diffusion equation:

$$\nabla\cdot(D\nabla C) = 0 \quad (1)$$

where D is the diffusion coefficient of oxygen in the corresponding material. Values of D were set to $D_{PDMS} = 3.25 \times 10^{-9}$ m^2 s^{-1} for PDMS and $D_{medium} = 2.00 \times 10^{-9}$ m^2 s^{-1} for the culture medium.

Boundary conditions were imposed such that the oxygen concentration on the outer PDMS surface above the normoxia zone was fixed to the ambient value of 21% O_2 at 37 °C, while the concentration on the outer PDMS surface above the hypoxia zone was set to zero to mimic complete nitrogen purging. All other external faces were modeled as zero-flux boundaries. Eqn (1) was solved on a three-dimensional mesh that included the PDMS walls and the six cell-culture chambers. The resulting spatial concentration field yielded a continuous oxygen profile throughout the device. Simulations were repeated for several distances between the hypoxic and normoxic zones.

Microfluidic system fabrication. The proposed microsystem consists of two PDMS layers: the bottom layer containing

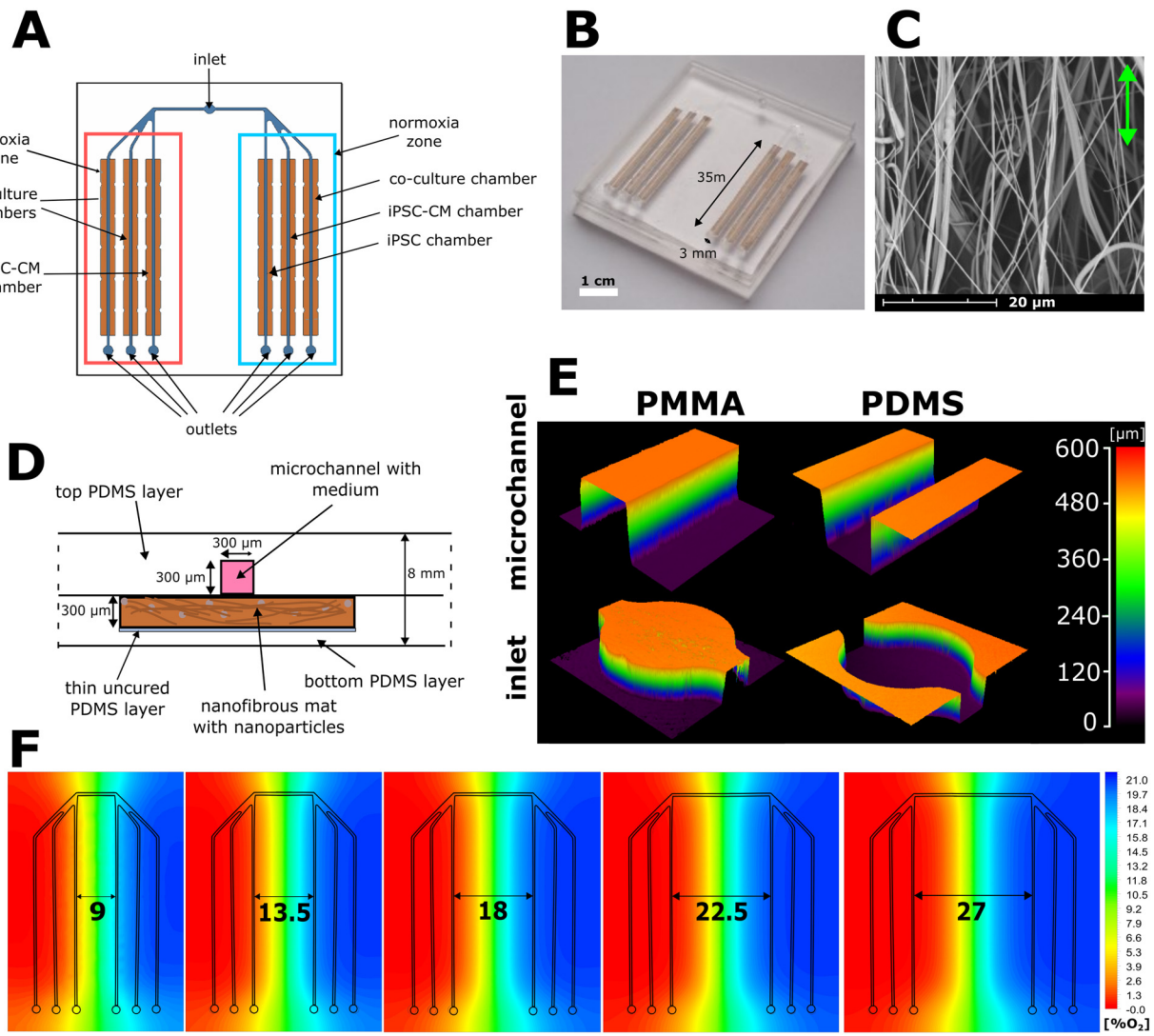

Fig. 2 Characterization of the designed microsystem. (A) A schematic overview of the microsystem. The microsystem consists of six microchambers with one inlet and six outlets. (B) A photo of the device without inlet and outlet tubes connected. (C) A SEM image of the PU nanofibrous mats integrated with magnetic Fe_3O_4 nanoparticles. The green arrow indicates the direction of the flow in the microchannels. (D) A schematic cross-section of the microchamber and the microfluidic channel. (E) Laser microscope images of the microstructures in the PMMA stamp and PDMS cast. (F) Computer simulations of oxygen concentrations throughout the microsystem. Based on these images and quantitative data collected from the simulations, a distance of 22.5 mm between the two middle microchannels was chosen.

microchambers and the top layer containing microchannels with an inlet and outlets. There are 6 microchambers (35 mm × 3 mm × 0.3 mm), integrated with nanofibrous mats, each with a separate microchannel (0.5 mm × 0.5 mm), outlets, and one combined inlet (Fig. 2A and B). Three of the microchambers are subjected to hypoxic conditions, and three remain in normoxia, therefore creating a 'hypoxia zone' and a 'normoxia zone'. Each microchamber has different cell cultures in later experiments, such as iPSC culture, iPSC-CM culture, and iPSC/iPSC-CM co-culture. Previously described[33] polyurethane (PU) nanofibrous mats with magnetic Fe_3O_4 nanoparticles were integrated into the microchambers (Fig. 2C).

The PDMS–PDMS microsystem was made using poly(dimethylsiloxane) (PDMS) casting The mold was fabricated by milling a 6 mm thick poly(methyl methacrylate) (PMMA) block. Two cylindrical flat cutters (of diameter 3.175 mm and 1 mm) were used to replicate the chambers and channels in PMMA. The microstructures were milled into a PMMA sheet creating two separate molds – for the top and bottom PDMS layer. Both layers were cast in PDMS and, together with the PMMA mold, imaged with a LEXT laser microscope to verify the dimensions of the microstructures (Fig. 2E).PDMS was prepared in a ratio of 10 : 1 elastomer base to curing agent (SYLGARD™), degassed, poured into the mold, and cured for 1 h at 75 °C. After curing, the two layers of PDMS were cast from the mold. Inlets and outlets were drilled into the top layer with a 1.5 mm drill.

The device was integrated with polyurethane (PU) nanofibrous mats with iron(II, III) oxide (Fe_3O_4) magnetic nanoparticles, which

have been described in detail in our previous work.[33] In short, the nanofibrous mats, which were fabricated by solution blow spinning (SBS), contain magnetic nanoparticles used to stimulate the cell culture mechanically. When placed between two magnets that move up and down, the mats (and cells adhered to the nanofibers) move periodically, stimulating uniform contractions of cells in the culture. Nanofibrous mats were laser cut to the size of the chambers and attached to the bottom PDMS layer with a thin layer of uncured PDMS. Both layers were then placed on a glass sheet and warmed for 10 min at 75 °C. Immediately after, microsystems were formed by bonding two PDMS layers using an oxygen plasma generator (Diener Electronic Atto) and left in the oven at 75 °C for 30 min. After bonding, the nanofibrous mats in the chambers were modified with polydopamine (PDA). The polymerization of dopamine hydrochloride to polydopamine in the chamber aids the adhesion of cells.[43] For this, a 2 μg ml^{-1} of dopamine hydrochloride in Tris-HCl (pH 8.4) was streamed into all the chambers and incubated for at least 24 h at RT. For sterilizing before cell culture, the devices were submerged in water, degassed with a vacuum pump, and placed in an autoclave for 1 h at 121 °C.

Design and fabrication of the hypoxia holder. The holder for generating hypoxic conditions in the microfluidic device was designed using Autodesk Fusion 360. The holder consisted of two PMMA layers and an aluminum plate that served as a heat-conducting material to distribute the heat from a commercial

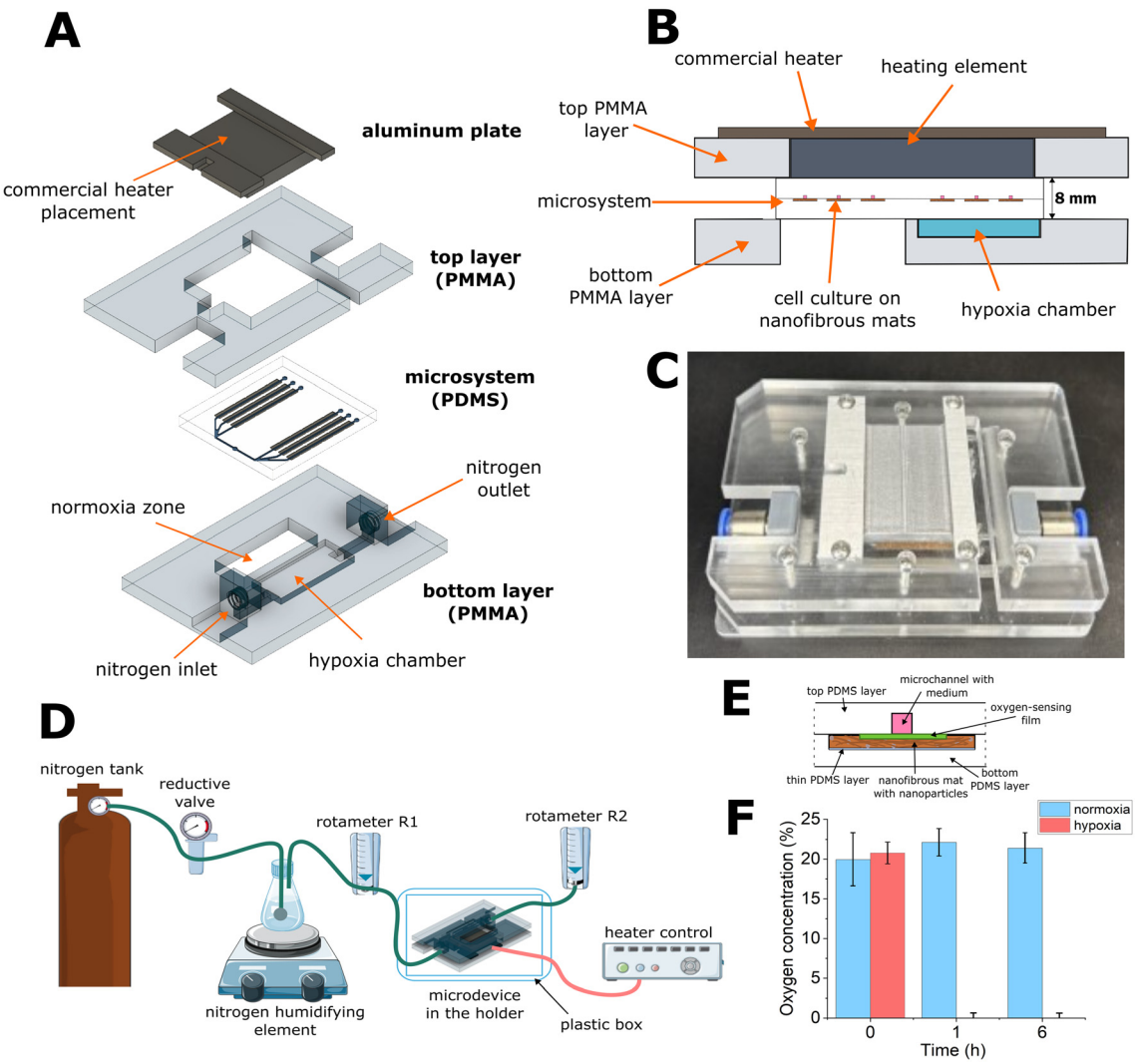

Fig. 3 Hypoxia holder and hypoxia setup development. (A) Four layers of the hypoxia holder. The hypoxia chamber was sealed with two layers of PMMA with a PDMS microsystem in between. The aluminum plate was used to distribute heat evenly throughout the microsystem. (B) A cross-section of the hypoxia holder with the microsystem placed inside. (C) A photo of the hypoxia holder with 6 screws placing it together, 4 screws attaching the aluminum plate and 2 quick connectors placed in the nitrogen inlet and outlet. (D) A diagram of the whole hypoxia setup, where the nitrogen flows from the tank through a humidifying element to the hypoxia holder and is controlled by a reducer and two rotameters. (E) A schematic cross-section of the microchamber and the microfluidic channel showing the location of the oxygen-sensing film. (F) Oxygen concentrations in the cell culture chambers after 0, 1, and 6 h of generating hypoxic conditions in the hypoxia holder.

heater evenly throughout the microsystem. The two PMMA layers were fabricated by milling PMMA sheets, similarly to the device mold. Nitrogen was supplied through a 3D-printed inlet glued to the bottom PMMA layer. The microsystem was secured in the holder, with the two PMMA layers squeezing the microsystem and sealing the hypoxia chamber in the holder (Fig. 3A–C). The holder's dimensions are 128 mm × 85 mm × 22 mm, making it compatible with a standard plate reader to allow for easy on-chip experiments.

The setup for generating hypoxic conditions consisted of a nitrogen tank, connected to a regulator, a nitrogen humidifying element, a rotameter R1 (to control the nitrogen flow before the inlet into the hypoxia chamber in the holder), a holder with the microsystem and a rotameter R2 (to control the nitrogen flow after the hypoxia chamber) (Fig. 3D). The two rotameters serve as nitrogen leakage control. The nitrogen cylinder regulator was connected by a tube to the humidifying module (a tube with an aquarium aeration stone submerged in water). The microsystem secured in the holder was placed in a transparent plastic box to limit fluctuations of external conditions, such as humidity and temperature. For experiments, hypoxia was maintained in an active state for 6 h.

Hypoxia verification. Hypoxic conditions were verified with the use of an oxygen-sensing film SF-RPSu4-L4/W4/OIW (Presens). This material quantifies oxygen levels based on radiometric luminescence imaging (RLI). The primary sensing layer consists of a platinum tetrakis(penta-fluorophenyl)porphyrin (PtTFPP) complex (ex 400 nm/em 650 nm). The fluorescence intensity of the platinum complex is being quenched with the increase of oxygen concentration. The second layer of the film is a reference dye (em 510 nm), which does not react with oxygen, allowing for calibration. Both layers are set on an additional polymer layer to prevent noise caused by environmental oxygen. Before measurement in the microsystem, a calibration curve for the foil was created. A small piece of the film was bonded between two square 5 mm thick layers of PDMS. The bonded foil was placed in a commercial-grade incubator for 24 h, set to different oxygen concentrations at a time (1, 6, 11, 16, and 21%). Later, the foil was quickly transferred to a plate reader (Biotek, Cytation3) for measurement, which was taken continuously for 1 min, to verify the stability of fluorescence. A calibration curve was created from the collected data.

A 3 mm × 3 mm piece of sensing film was placed in each culture chamber in the microsystem to verify hypoxia generation efficiency and the stability of hypoxic conditions. After introducing culture medium to all microchambers, the microsystem was placed in the hypoxia holder for 6 h, hypoxic conditions were induced, and fluorescence measurements were taken in a plate reader using a spectrofluorometer at 0, 1, and 6 h.

Routine cell culture. Human induced pluripotent stem cells (iPSCs, IIMCBi001-A (ELE10) line) were obtained from the Laboratory of Molecular and Cellular Neurobiology of the International Institute of Molecular and Cell Biology in Warsaw.[44] The cells were cultured on 6-well plates coated with Matrigel® (Corning). Differentiation of iPSCs to iPSC-derived cardiomyocyte-like cells (iPSC-CMs) was done according to the GiWi protocol.[20] IPSC-CMs were seeded in RPMI medium with 20% v/v fetal bovine serum (FBS, Gibco), 1% v/v 100 mM penicillin–streptomycin (Sigma-Aldrich), and 5 μM ROCK inhibitor and cultured in RPMI medium with B-27 supplement with insulin (Gibco) and 1% v/v 100 mM penicillin–streptomycin with medium changes every two days. The cultures were maintained in a humidified incubator (37 °C, 5% CO_2).

Cell culture in microsystems. After microsystem sterilization, the culture medium was supplemented with 200 mM HEPES (Gibco) as a CO_2 buffering agent, introduced into the microsystem, and incubated (37 °C, 30 min) before cell seeding. The cells (at the concentration of 1×10^6 cells per ml) were introduced through the inlet into the microchambers with a flow of 15 μl min^{-1} with a peristaltic pump (Ismatec). Next, the microsystem was incubated for 48 h to allow the cells to attach. After that time, hypoxia (1% of oxygen concentration) was induced for 6 h, and cell viability and functionality were analysed.

Assessment of ATP levels in cells. ATP levels in cells after hypoxia were determined using the CellTiter-Glo® 2.0 Cell Viability Assay (Promega). Before the assay, the CellTiter-Glo® 2.0 reagent was diluted 1 : 1 in culture medium (RPMI + B-27). This solution was introduced into the culture chambers with a 100 μl min^{-1} flow rate for 1 min through the inlet. The lysates were collected from the outlets into 1.5 ml tubes. The microsystems were then covered with aluminum foil and incubated (30 min, RT). Then, the chambers were flushed again with the CellTiter-Glo® 2.0/medium solution. Lysates were collected into the same tubes as previously, and 100 μl of the lysates were transferred to a 96-well plate. The bioluminescent signal was measured in a plate reader (BioTek Cytation3) with the reagent/medium mixture as a negative control, and ATP levels were determined.

JC-1 staining. The mitochondrial membrane potential of the cells was measured using the JC-1 dye (Thermo Fischer Scientific). JC-1 is a carbocyanine dye that exhibits green fluorescence at low concentrations (as a monomer) and red fluorescence at high concentrations (aggregates). When added to the culture, the amount of dye penetrating the mitochondrial membrane depends on the membrane potential. The mitochondrial membrane potential is quantitatively determined by calculating the ratio of red fluorescence intensity (ex 535 nm/em 590 nm) to green fluorescence intensity (ex 485 nm/em 530 nm). The dye in a 10 μg ml^{-1} concentration was introduced into each culture chamber through the inlet at a flow rate of 15 μl min^{-1}. Next, the microsystem was incubated in the dark (20 min, RT) and imaged with fluorescence microscopy (Olympus IX71 with a Hamamatsu Orca-spark camera). Finally, the images were analyzed using ImageJ software and a designed algorithm to quantify the fluorescence intensity.

Calcein-AM and propidium iodide staining. Calcein-AM (CAM) and propidium iodide (PI) staining were performed to

differentiate living and dead cells. A mixture of the dyes was prepared in the culture medium with final concentrations of 5 μg ml^{-1} calcein-AM and 2 μg ml^{-1} propidium iodide. The solution was vortexed (Labnet VX100), introduced into the chambers of the microsystem, and incubated in the dark (10 min, RT). After that, the cells were observed using a fluorescence microscope (Olympus IX71 with a Hamamatsu Orca-spark camera). The images were analyzed using ImageJ software.

The study aimed to differentiate between living and dead cells. In a dark 2 ml centrifuge tube, a dye mixture in the culture medium was prepared, maintaining the proportions of 1 μl of calcein-AM (CAM) at a concentration of 2 mM (Sigma-Aldrich) and 2 μl of propidium iodide (PI) at a concentration of 1 mg ml^{-1} (Sigma-Aldrich) per 1 ml of medium (final concentrations of CAM and PI were 2 μM and 2 μg ml^{-1}, respectively). The dye mixture was vortexed (Labnet VX100) and introduced into the microsystem (10 μl min^{-1}, 2 min per channel). After incubation (3 min), the cells were observed using an inverted fluorescence microscope (Olympus IX71). The study was conducted for 1, 3, and 5 days of culture for both stimulated and non-stimulated cells.

Co-culture of iPSC-CMs after hypoxia with iPSCs. The initial stages of preparing the co-culture were the same as for culturing iPSC-CMs. iPSC-CMs were introduced into the microsystem and put under hypoxia, as previously. After 6 h, the microsystem was removed from the hypoxia setup. Fresh RPMI/B-27 medium was introduced, and the microsystem was incubated (30 min, 37 °C). An iPSC cell suspension was prepared at a 1×10^6 cells per ml density and introduced into the device at a flow rate of 15 μl min^{-1} with a peristaltic pump (Ismatec). The cells were co-cultured for 5 days, with the medium in the chambers being changed every 2 days and daily mechanical stimulation. Details of the mechanical stimulation are described below.

Cell labelling with a CellTracker dye. Before introducing iPSCs into the microsystem, the culture was labelled with CellTracker™ Red CMTPX Dye (ThermoFischer Scientific). The dye was used in the highest recommended concentration of 25 μM to allow for long-term fluorescent cell culture. The cells were dyed on a 6-well culture plate, then dissociated, counted, and introduced into the microsystem.

Mechanical stimulation. A magnetic field generator described in a previous publication was used for mechanical stimulation. In short, the device consists of two neodymium magnets, between which the microsystems are placed. As the magnets move up and down, the magnetic nanoparticles in the nanofibers move as well, and the rhythmic stretching of the nanofibers aids the movement of the cells themselves. This way, the cells are stimulated to contract in a uniform manner, mimicking native heart muscle. The cell cultures were mechanically stimulated for 5 days, 1 h daily, with a frequency of 0.5 Hz. Our team's previous work describes the principle of mechanical stimulation treatment.[45]

Immunostaining. Immunostaining was chosen as a method to visualize changes in the iPSC/iPSC-CM co-culture after mechanical stimulation. Cardiac troponin T (cTnT) was stained, a contractile protein abundant in healthy cardiomyocyte cells. The procedure was conducted according to a basic indirect immunostaining protocol, with the solutions being introduced to the microchambers with a peristaltic pump. The cell culture was rinsed with DPBS and fixed with 4% paraformaldehyde for 40 min. Then, the cells were permeabilized with 0.5% Triton X and blocked for 1 h with 2.4% BSA in 0.5% Triton X. The rabbit monoclonal anti-troponin T primary antibody (Abcam) was introduced into all microchambers of the microsystem and incubated overnight at 4 °C. The next day, the cells were rinsed with 0.1% Triton X and incubated for 1 h with a secondary goat anti-rabbit antibody conjugated with Alexa488 (Thermo Fischer Scientific). After that, the cultures were stained with Hoechst. Immediately before imaging, the bottom PDMS layer of the microsystem was separated from the top layer and placed on a thin glass slide with a few drops of water. The cultures were imaged using confocal microscopy (Olympus).

Statistical analysis. Each experiment was conducted at least 3 times. All obtained data were expressed as the mean ± standard deviation (SD). Statistical analysis was performed using one-way analysis of variance (One-Way ANOVA). *P*-Values of <0.05 were considered statistically significant.

Results and discussion

Heart-on-a-chip microsystem development

Different distances between the hypoxia and normoxia zones were considered during the microsystem design process. It was important to optimize this parameter since PDMS is highly permeable to oxygen, and there should be no diffusion of oxygen between the two zones, resulting in a clear difference between in the zones. In numerical simulation experiments, the mean oxygen concentration value for a 9 mm gap equaled (respectively for the hypoxia and normoxia zone) 1.9% ± 1.5% and 19.3% ± 1.4%; for the 13.5 mm gap – 1.1% ± 0.9% and 20.2% ± 0.7%; for the 18 mm gap – 0.6% ± 0.5% and 20.4% ± 0.5%; for the 22.5 mm gap – 0.3% ± 0.3% and 20.7% ± 0.3%; and for the 27 mm gap – 0.2% ± 0.2% and 20.8% ± 0.2% (Fig. 1D). The distance between zones was chosen based on the standard deviation values for both zones. As a result of the simulations, a 22.5 mm gap was chosen, as it allowed for a significantly smaller SD value than the 18 mm gap, but there was no significant improvement in the homogeneity between the 22.5 and 27 mm gaps (Fig. 2E).

LEXT microscopy imaging revealed no significant differences between the measurements of the design, mold, and cast, which confirmed the high quality of the device fabrication method. For example, the widths of the microchannel and microchamber in the cast were respectively equal to 495.0 ± 1.5 μm and 2930 ± 6 μm compared to 500 μm and 3000 μm in the design. Finally, the microsystems were bonded with oxygen plasma, and later the nanofibrous mats were modified with polydopamine to increase their hydrophilicity.[46]

Hypoxia holder design and fabrication

A custom holder was designed to achieve hypoxic conditions in three of the microchambers (Fig. 3). The holder consisted of two PMMA layers between which the microsystem was inserted and an aluminum plate (attached with four 18 mm M3 screws), which was specifically made to fit a custom designed 71 mm × 20 mm × 3.5 mm commercially available heating element based on a JUMO eTRON M controller. The holder dimensions with the microsystem attached but without the aluminum plate are 128 mm × 85 mm × 22 mm. The aluminum plate is responsible for even heat conduction throughout the microsystem, and it is removable to allow for in-holder measurements (since aluminum is opaque and cell cultures cannot be imaged or measured through it). The bottom PMMA layer had a cavity milled on one side with an inlet and an outlet, which accounted for the hypoxia chamber (Fig. 2A–C). The top layer served mostly as a holder for the placement of a heating element but also helped to squeeze the microsystem against the bottom layer, thus creating a tightly sealed hypoxia chamber. With nitrogen constantly flowing through the hypoxia chamber (at a flow rate of 50 Nl h^{-1}), an anaerobic environment was created in the hypoxia chamber in the holder, which encouraged a gas exchange between the hypoxia chamber and microchambers in the hypoxia zone in the microsystem. Consequently, the oxygen in the microchambers was replaced by nitrogen until the oxygen concentration reached ~1%.

The hypoxia setup consisted of a nitrogen tank, from which the nitrogen flows to the nitrogen humidifying and heating element (Fig. 3D). This is made of a glass bottle filled with water, into which a nitrogen tube is attached, finished with an aeration stone. The bottle was put on a heating block. Next, the nitrogen flows through a rotameter to the hypoxia holder. Another rotameter is installed after the holder, which allows checking for any nitrogen leaks through the setup.

An experiment with an oxygen-sensing film SF-RPSu4-L4/W4/OIW (Presens) was conducted to verify the ability to induce hypoxia in the setup. It was observed that after 1 h the level of oxygen in the hypoxia zone reached a level of around 0%, and it stayed at this level after 6 h, while the level of oxygen in the normoxia zone remained at a value of around ~21% the whole time (Fig. 3E). This result confirmed that the designed microsystem is suitable for inducing hypoxia in cell culture.

Cell culture under hypoxia

The next part of the work was to determine how an iPSC-CM cell culture would behave after exposure to hypoxia in the developed microsystem. In *in vivo* conditions during a heart attack and hypoxia of the myocardium, cardiomyocytes suffer great damage, which may lead them into the apoptosis pathway. This causes metabolic changes, such as ATP production and mitochondrial potential. Assessed with a luminescence-based assay, after 6 h of hypoxia, there was a significant decrease (37%) in the ATP concentration within the iPSC-CM culture compared to the control normoxic culture (Fig. 4A). It was observed that during a prolonged period of hypoxia the cells limit ATP production. This result shows that hypoxia was successfully maintained in the cell culture and impacted ATP production, similarly to *in vivo* conditions.

CAM/PI staining revealed that there is no largely significant, but a small increase in the number of dead cells in the culture after hypoxia. It was hypothesized that the 6 h hypoxia in the hypoxia setup does not instantly cause cells to die by necrosis, but damages them significantly and triggers apoptosis pathways, which causes their intracellular processes to slow down (Fig. 4B). What else can be seen in this staining is that the live cells exhibit a uniform arrangement that is parallel to the direction of the nanofibrous mats in the microchambers.

To test the mitochondrial activity, the JC-1 staining was conducted. JC-1 is a carbocyanine dye, which in its monomer state, exhibits green fluorescence, while in high concentrations, forms aggregates, which cause a fluorescence wavelength shift to red. In active mitochondria (with a high membrane potential), the dye is transported inside the mitochondrial membrane in big quantities, achieving high concentrations and forming red fluorescent aggregates. The dye remains in a monomer form in mitochondria with low membrane potential. This assay quantifies the mitochondrial membrane potential as a red to green fluorescence intensity ratio. After 6 h of hypoxia, a reduction in the red/green fluorescence ratio from 3.31 ± 0.22 to 2.24 ± 0.41 ($n = 3$, $p < 0.01$) was observed (Fig. 4C and D). There is a significant loss of mitochondrial membrane potential due to hypoxia-induced stress. This, along with the limitation of ATP production and CAM/PI staining, accounts for the conclusion that the microsystem, hypoxia holder, and setup are a feasible tool to conduct cardiac hypoxia research.

iPSC-CM and iPSC co-culture after hypoxia and mechanical stimulation

One of the benefits of the developed microfluidic device is the possibility of conducting multiple variants of cell culture in a single device. Therefore, in the studies on the co-culture of iPSC-CM and iPSC, the cells were introduced into the culture chambers as shown in the diagram in Fig. 2A. To start the co-culture, iPSC-CMs were introduced into five of the six microchambers (iPSC-CM and co-culture microchambers as described in Fig. 2A), cultured in the microsystem, and subjected to hypoxia as was described before. After hypoxia, iPSC cells labeled with CellTracker Red CMFDA were introduced into four of the six microchambers (co-culture and iPSC microchambers as shown in Fig. 2A).

Mechanical stimulation treatment was implemented after 24 h of co-culture of hypoxic iPSC-CM cells with iPSC cells. It was carried out for 1 h daily for 5 days in a magnetic field generator described in our previous work.[45] Mechanical stimulation, previously shown to promote cardiomyocyte maturation,[45] was

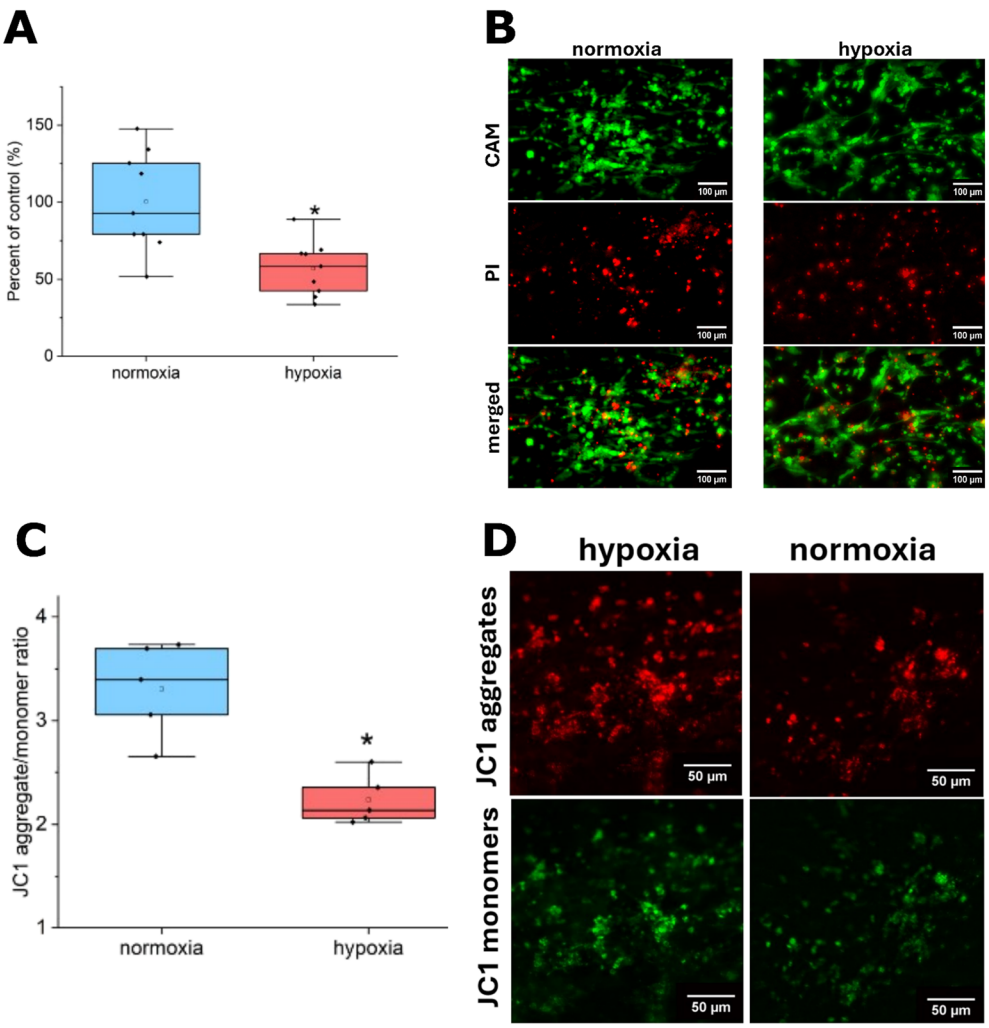

Fig. 4 (A) ATP levels in the normoxic and hypoxic iPSC-CM cultures after 6 h of hypoxia. (B) CAM/PI staining of the cultures. (C and D) Results of JC-1 staining of the cultures. *$p < 0.05$.

applied to investigate its effects on hypoxic and normoxic iPSC-CMs in co-culture with iPSCs.

A day after the last day of mechanical stimulation treatment, the cardiac troponin T (cTnT) level was examined. Troponins are a family of proteins that play a crucial role in the contractions of muscles, and cTnT is a type of troponin specific to the heart muscle. Due to its specificity, it is commonly used as a cardiomyocyte marker for staining. The presence of cTnT in the culture, especially in the iPSCs, would suggest that iPSCs gain cardiomyocyte-like properties, indicating the initiation of their differentiation toward cardiomyocytes. This, in turn, would imply that our designed setup can be implemented in cardiac regeneration studies, toward personalized stem cell therapies. In the staining, the iPSC-CM monoculture exhibited the presence of cTnT (green) under both normoxic and hypoxic conditions, as can be expected for mature cardiomyocytes (Fig. 5). The cells exhibited mainly an elongated shape, and perpendicular stripes of cTnT can be seen throughout the cells. We also noticed that in the hypoxic iPSC-CM monoculture, some of the cells presented a rounded shape, which can indicate cardiomyocyte cell damage due to hypoxia. Interestingly, in the co-culture of iPSCs with normoxic iPSC-CMs, it was observed that iPSCs (marked in red) closely adhered to cardiomyocytes. Characteristic stripes of cTnT are present in the iPSC-CMs, and some small cTnT are visible in iPSCs (Fig. 5). This indicates that close adhesion of iPSCs to iPSC-CMs can be a factor in initiating cardiac differentiation in cardiomyocytes. Nevertheless, the level of cTnT in iPSCs in co-culture with normoxic iPSC-CMs is low, and evident cTnT stripes are not present. In the co-culture of iPSCs with hypoxic iPSC-CMs, a distinct presence of cTnT was noted in the stem cells, but cell adhesion was not apparent, differing from the coculture with normoxic iPSC-CMs. iPSCs in this culture exhibited smaller nuclei and their shape was elongated, however, not as much as a typical cardiomyocyte shape. These results might indicate that in co-culture with both hypoxic and normoxic iPSC-CMs, the process of differentiation into cardiomyocytes was initiated in iPSCs, although in the co-culture with hypoxic iPSC-CMs, this

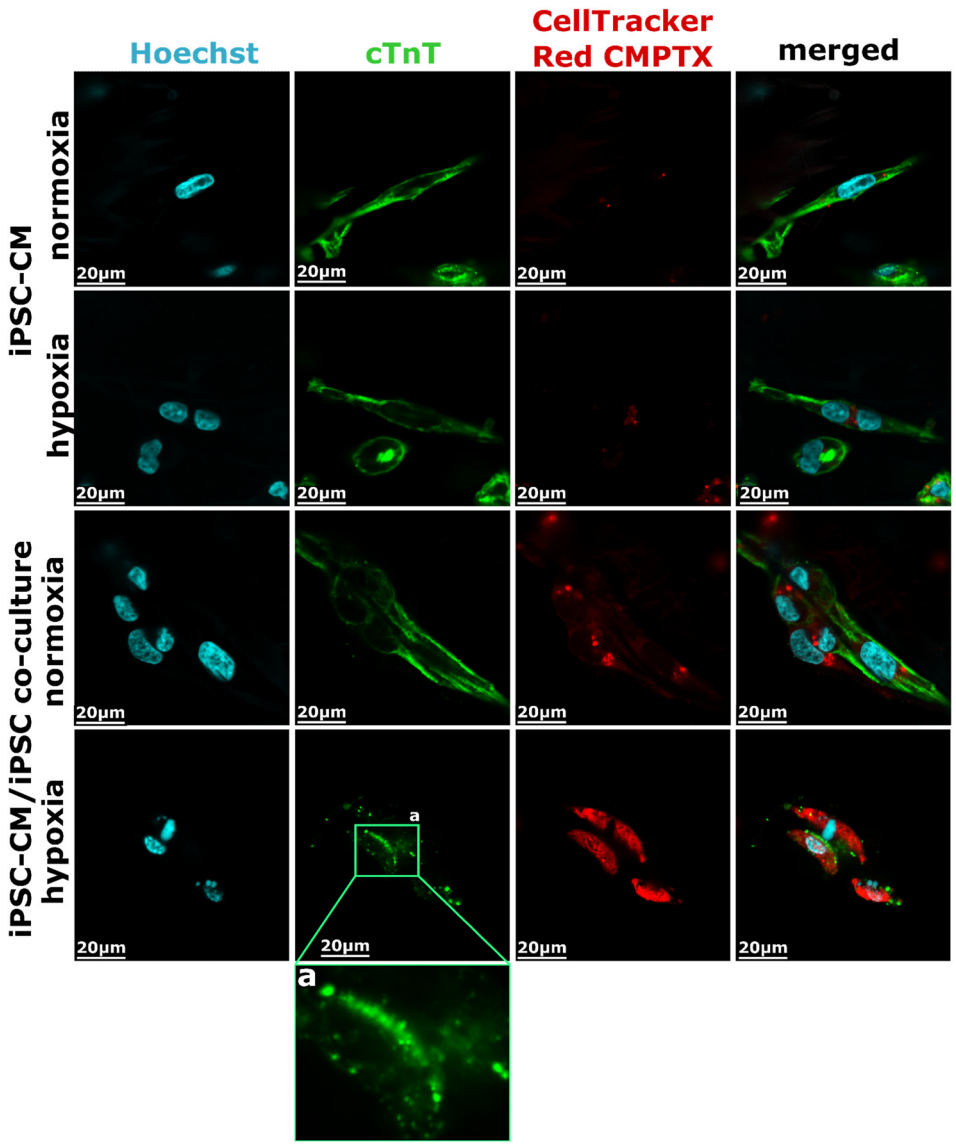

Fig. 5 Immunostaining of the different types of cultures. iPSCs were stained with CellTracker red CMPTX before being introduced into the co-culture with normoxic or hypoxic iPSC-CMs. After 5 days of mechanical stimulation in the magnetic field generator, the cultures were stained with cTnT and Hoechst. In the normoxic iPSC-CM/iPSC co-culture. (a) A closer image of cTnT stripes in iPSCs in hypoxic iPSC-CM/iPSC co-culture.

process is more visible. To verify this conclusion, more research is needed, as these results are only qualitative and require further validation. Nevertheless, it can be observed that iPSCs cultured in the presence of cardiomyocytes (subjected to hypoxia or not), may initiate differentiation toward cardiomyocytes.

Discussion

In this study, we developed a heart-on-a-chip microsystem capable of inducing localized hypoxia in cardiomyocyte cultures, effectively modeling ischemic conditions *in vitro.* Hypoxic and normoxic zones were created successfully, as was confirmed by oxygen-sensing measurements. It can be a valuable platform for studying cellular responses to hypoxia, particularly in cardiac ischemia. Our findings demonstrated a significant decrease in ATP levels (by 37%) and mitochondrial membrane potential (by 32%) in iPSC-derived cardiomyocytes (iPSC-CMs) after 6 hours of hypoxia, without a corresponding increase in cell death. This indicates substantial metabolic stress induced by hypoxia.

These results align with several previous studies showing that hypoxia leads to metabolic alterations in cardiomyocytes. Multiple researchers have reported that hypoxia impairs mitochondrial function and ATP production, leading to energy deficits that compromise cell function without immediate cell death.[47–51] For instance, Neubauer *et al.*[52] and Murphy *et al.*[53] observed decreased ATP levels and impaired contractility in cardiomyocytes under hypoxic conditions, while Di Lisa *et al.*[54] and Solaini *et al.*[55] demonstrated that hypoxia induces mitochondrial depolarization and disrupts energy metabolism in cardiac cells. Collectively, these studies

support our observation that hypoxia leads to significant metabolic stress in cardiomyocytes without causing immediate cell death. The lack of a significant increase in cell death, as evidenced by calcein-AM/propidium iodide staining, suggests that short-term hypoxia induces reversible metabolic changes rather than irreversible damage. In contrast, prolonged hypoxia may eventually lead to cell death through necrosis or apoptosis, as documented in longer-term studies.[47,56,57] Kalogeris *et al.*[47] and Muntean *et al.*[56] reported that extended hypoxic exposure results in increased apoptotic markers and loss of cell viability in cardiomyocytes. Martin[57] demonstrated that sustained hypoxia causes irreversible mitochondrial damage and cell death. These studies highlight the importance of hypoxia duration in determining cell fate, emphasizing that while short-term hypoxia may be reversible, prolonged hypoxic conditions can lead to irreversible cellular damage.

The alignment of iPSC-CMs parallel to the direction of flow within the microchambers highlights the influence of the microfluidic environment on cellular organization. Shear stress induced by laminar flow and the rectangular geometry of the microchambers likely contributed to this alignment, promoting a more physiologically relevant tissue architecture. Similar observations have been made by other researchers, demonstrating that shear stress and microenvironmental cues enhance engineered cardiac tissues' structural and functional maturation.[58–61] For instance, Carlos-Oliveira *et al.*[59] showed that shear stress and mechanical stimulation improve cardiomyocyte alignment and functionality. Vivas *et al.*[60] and Liu *et al.*[61] also found that controlled shear stress in microfluidic systems promotes cardiomyocyte alignment and maturation, enhancing tissue functionality.

The integration of nanofibrous mats composed of polyurethane with embedded magnetic Fe_3O_4 nanoparticles provided both structural support and mechanical stimulation. Mechanical stimulation has been shown to promote cardiomyocyte maturation, enhance sarcomere organization, and improve contractile function.[62–65] The use of magnetic nanoparticles allowed for controlled mechanical stretching, simulating the dynamic mechanical environment of the native myocardium. Studies by Ruan *et al.*[62] and Shi *et al.*[63] support this approach, demonstrating that mechanical conditioning improves the maturation and functionality of cardiomyocytes *in vitro*.

These findings reinforce the effectiveness of mechanical stimulation in promoting cardiomyocyte maturation, validating the design of our microsystem. Our microsystem offers several advantages for cardiac tissue engineering and disease modeling. The ability to induce localized hypoxia allows for the study of ischemia-related cellular responses in a controlled setting, which is crucial for understanding the pathophysiology of myocardial infarction. Additionally, the combination of hypoxia with mechanical stimulation provides a more comprehensive simulation of the *in vivo* cardiac environment, potentially leading to more predictive models for drug testing and therapeutic development.

While our device effectively models hypoxic conditions and allows for mechanical stimulation, there are limitations to consider. The study focused on short-term hypoxic exposure; thus, the long-term effects of hypoxia and potential reperfusion injury upon reoxygenation were not assessed. Future studies should investigate the cellular responses during more extended hypoxic periods and upon reoxygenation to better mimic ischemia–reperfusion injury, a critical aspect of myocardial infarction.[66–68] Moreover, while we assessed metabolic function and viability, additional functional analyses such as contractility measurements, electrophysiological assessments, and gene expression profiling would provide deeper insights into the impact of hypoxia and mechanical stimulation on cardiomyocyte function and maturation. Studies by Gaitas *et al.*,[69] Qian *et al.*,[70] and Marsano *et al.*[71] have shown that these analyses are crucial for evaluating cardiomyocyte maturation and functionality. Our results indicate that co-culturing iPSCs with hypoxia-damaged iPSC-CMs may stimulate the differentiation of iPSCs into cardiomyocyte-like cells, as evidenced by the expression of cardiac troponin T in the co-cultured iPSCs (Fig. 5). The observed differences may be attributed to molecular pathways specifically activated under hypoxic stress. Stabilization of HIF-1α in hypoxic cardiomyocytes can alter their secretome, increasing the release of paracrine factors such as VEGF, IGF-1, and HGF, which have been shown to promote cardiac lineage commitment of stem cells through PI3K/Akt and MAPK signaling.[72,73] Moreover, hypoxia has been reported to directly prime stem cells toward cardiomyogenic differentiation by upregulating transcription factors including NKX2-5 and GATA4.[74,75] These mechanisms could underlie the more pronounced cTnT expression we observed in iPSCs co-cultured with hypoxic cardiomyocytes compared with normoxic conditions, suggesting that the hypoxic microenvironment provides stronger cues for initiating cardiomyocyte-like differentiation. This suggests that hypoxic cardiomyocytes may release paracrine factors that promote cardiomyogenic differentiation of neighboring stem cells. Similar findings have been reported in previous studies, where the microenvironment created by damaged cardiomyocytes enhances stem cell differentiation and cardiac repair.[76,77] For instance, Menasché *et al.*[78] demonstrated that transplantation of human embryonic stem cell-derived cardiovascular progenitors improved cardiac function in patients with severe ischemic heart disease. Laflamme *et al.*[79] showed that human embryonic stem cell-derived cardiomyocytes enhanced the function of infarcted rat hearts when combined with pro-survival factors. Additionally, Matsa *et al.*[80] reviewed the potential of human stem cells in modeling heart disease and their role in regenerative therapies. Our findings align with these studies, suggesting that co-culturing iPSCs with hypoxia-injured cardiomyocytes may be a promising strategy for promoting cardiac regeneration.

Conclusions

We have developed a novel heart-on-a-chip system that enables the study of cardiomyocyte responses to hypoxia and mechanical stimulation in a controlled microenvironment.

The device effectively simulates ischemic conditions and provides structural and mechanical cues that promote cellular alignment and maturation. Our findings demonstrate that short-term hypoxia induces significant metabolic stress in iPSC-CMs without immediate cell death, underscoring the importance of timely therapeutic intervention in ischemic heart disease. Importantly, we observed that co-culturing iPSCs with hypoxia-damaged iPSC-CMs may stimulate the differentiation of iPSCs into cardiomyocyte-like cells, as evidenced by the expression of cardiac troponin T in the co-cultured iPSCs. This suggests that hypoxic cardiomyocytes may release paracrine factors promoting cardiomyogenic differentiation of neighboring stem cells, highlighting a potential cardiac repair and regeneration mechanism. This platform holds significant potential for advancing cardiac tissue engineering, disease modeling, and the development of new treatments for cardiac ischemia and related conditions. By providing a versatile tool to study the complex interactions between hypoxia, mechanical stimulation, and stem cell differentiation, our microsystem could contribute to the development of novel regenerative therapies for ischemic heart disease.

Author contributions

Conceptualization – JE, KD, SA; data curation – KD, SA, ISZ; formal analysis – KD, SA; funding acquisition – JE; investigation – JE, SA, KD, ISZ, WM, DM; methodology – JE, SA, KD, ISZ, WM, DM; project administration – JE; resources – JE; software – KD; supervision – JE; validation – KD, SA, JE; visualization – SA; writing – original draft – SA, KD; writing – review & editing – JE, WM, DM, ISZ.

Conflicts of interest

The authors would like to note that there are no conflicts of interests to declare.

Data availability

Data for this article, including dataset are available at "A novel holder and microfluidic system for spatially controlled hypoxia induction, mechanical stimulation and cardiac regeneration research" at **https://doi.org/10.5281/zenodo.15357007**.

Acknowledgements

This work is supported by the National Science Centre within the framework of the SONATA BIS 9 Program No. 2019/34/E/ST5/00381. The monochromatic camera for microscopic pictures caption was purchased under the Research University Excellence Initiative Project, Priority Research Area, Biotechnology and Biomedical Engineering Research Center – BIOTECHMED-LAB 1 Project No. 504/04496/1020/45.010423. The authors would like to thank Dr. Ewa Liszewska and Prof. Jacek Jaworski from the Laboratory of Molecular and Cellular Neurobiology of the International Institute of Molecular and Cell Biology in Warsaw for providing access to iPSCs cell lines and Ewelina Krogulec, PhD, for additional help maintaining cell culture and the cardiomyocyte differentiation process. The authors would like to thank Prof. Artur Dybko, D.Sc. Ph. D. Eng. for the commercial heater delivery and Ph.D. Jakub Trzcinski for his help in analyzing the coating of nanofiber mats with polydopamine. The graphics in Fig. 1 and 3A were created using SMART Servier. The figures were created in Inkscape.

References

1 A. Wronska, *J. Pharmacol. Exp. Ther.*, 2023, **384**, 123–132.
2 M. M. Ahsan and Z. Siddique, *Artif. Intell. Med.*, 2022, **128**, 102289.
3 B. Godin, J. H. Sakamoto, R. E. Serda, A. Grattoni, A. Bouamrani and M. Ferrari, *Trends Pharmacol. Sci.*, 2010, **31**, 199–205.
4 S. M. Scott and Z. Ali, *Micromachines*, 2021, **12**, 319.
5 J. Fan, S. Li, Z. Wu and Z. Chen, in *Microfluidics for Pharmaceutical Applications*, ed. H. A. Santos, D. Liu and H. Zhang, William Andrew Publishing, 2019, pp. 79–100.
6 D. J. Beebe, G. A. Mensing and G. M. Walker, *Annu. Rev. Biomed. Eng.*, 2002, **4**, 261–286.
7 B. Sebastian and P. S. Dittrich, *Annu. Rev. Fluid Mech.*, 2018, **50**, 483–504.
8 L. A. Low, C. Mummery, B. R. Berridge, C. P. Austin and D. A. Tagle, *Nat. Rev. Drug Discovery*, 2021, **20**, 345–361.
9 R. Abdalkader and K. Kamei, *Lab Chip*, 2020, **20**, 1410–1417.
10 K. Ronaldson-Bouchard, K. Yeager, D. Teles, T. Chen, S. Ma, L. Song, K. Morikawa, H. M. Wobma, A. Vasciaveo, E. C. Ruiz, M. Yazawa and G. Vunjak-Novakovic, *Nat. Protoc.*, 2019, **14**, 2781–2817.
11 1P. Zamprogno, S. Wüthrich, S. Achenbach, G. Thoma, J. D. Stucki, N. Hobi, N. Schneider-Daum, C.-M. Lehr, H. Huwer, T. Geiser, R. A. Schmid and O. T. Guenat, *Commun. Biol.*, 2021, **4**, 1–10.
12 J. Yang, Y. Hirai, K. Iida, S. Ito, M. Trumm, S. Terada, R. Sakai, T. Tsuchiya, O. Tabata and K. Kamei, *Commun. Biol.*, 2023, **6**, 1–14.
13 Z. Lin, Z. Li, E. N. Li, X. Li, C. J. Del Duke, H. Shen, T. Hao, B. O'Donnell, B. A. Bunnell, S. B. Goodman, P. G. Alexander, R. S. Tuan and H. Lin, *Front. Bioeng. Biotechnol.*, 2019, **7**, 411.
14 L. Amirifar, A. Shamloo, R. Nasiri, N. R. de Barros, Z. Z. Wang, B. D. Unluturk, A. Libanori, O. Ievglevskyi, S. E. Diltemiz, S. Sances, I. Balasingham, S. K. Seidlits and N. Ashammakhi, *Biomaterials*, 2022, **285**, 121531.
15 R. X. Z. Lu, B. F. L. Lai, T. Benge, E. Y. Wang, L. Davenport Huyer, N. Rafatian and M. Radisic, *Adv. Mater. Technol.*, 2021, **6**, 2000726.
16 J. Liu, K. Miller, X. Ma, S. Dewan, N. Lawrence, G. Whang, P. Chung, A. D. McCulloch and S. Chen, *Biomaterials*, 2020, **256**, 120204.
17 H. Liu, O. A. Bolonduro, N. Hu, J. Ju, A. A. Rao, B. M. Duffy, Z. Huang, L. D. Black and B. P. Timko, *Nano Lett.*, 2020, **20**, 2585–2593.

18 L. Ren, W. Liu, Y. Wang, J.-C. Wang, Q. Tu, J. Xu, R. Liu, S.-F. Shen and J. Wang, *Anal. Chem.*, 2013, **85**, 235–244.
19 M. Abulaiti, Y. Yalikun, K. Murata, A. Sato, M. M. Sami, Y. Sasaki, Y. Fujiwara, K. Minatoya, Y. Shiba, Y. Tanaka and H. Masumoto, *Sci. Rep.*, 2020, **10**, 19201.
20 X. Lian, J. Zhang, S. M. Azarin, K. Zhu, L. B. Hazeltine, X. Bao, C. Hsiao, T. J. Kamp and S. P. Palecek, *Nat. Protoc.*, 2013, **8**, 162–175.
21 S. Vučković, R. Dinani, E. E. Nollet, D. W. D. Kuster, J. W. Buikema, R. H. Houtkooper, M. Nabben, J. van der Velden and B. Goversen, *Stem Cell Res. Ther.*, 2022, **13**, 332.
22 A. van Mil, G. M. Balk, K. Neef, J. W. Buikema, F. W. Asselbergs, S. M. Wu, P. A. Doevendans and J. P. G. Sluijter, *Cardiovasc. Res.*, 2018, **114**, 1828–1842.
23 T. J. Kolanowski, M. Busek, M. Schubert, A. Dmitrieva, B. Binnewerg, J. Pöche, K. Fisher, F. Schmieder, S. Grünzner, S. Hansen, A. Richter, A. El-Armouche, F. Sonntag and K. Guan, *Acta Biomater.*, 2020, **102**, 273–286.
24 A. Kobuszewska, E. Tomecka, K. Zukowski, E. Jastrzebska, M. Chudy, A. Dybko, P. Renaud and Z. Brzozka, *SLAS Technol.*, 2017, **22**, 536–546.
25 K. Ronaldson-Bouchard, S. P. Ma, K. Yeager, T. Chen, L. Song, D. Sirabella, K. Morikawa, D. Teles, M. Yazawa and G. Vunjak-Novakovic, *Nature*, 2018, **556**, 239–243.
26 J. Kreutzer, M. Viehrig, R.-P. Pölönen, F. Zhao, M. Ojala, K. Aalto-Setälä and P. Kallio, *Biomech. Model. Mechanobiol.*, 2020, **19**, 291–303.
27 A. López-Canosa, S. Perez-Amodio, E. Yanac-Huertas, J. Ordoño, R. Rodriguez-Trujillo, J. Samitier, O. Castaño and E. Engel, *Biofabrication*, 2021, **13**, 035047.
28 F. Zhang, K.-Y. Qu, B. Zhou, Y. Luo, Z. Zhu, D.-J. Pan, C. Cui, Y. Zhu, M.-L. Chen and N.-P. Huang, *Biosens. Bioelectron.*, 2021, **179**, 113080.
29 A. López-Canosa, S. Perez-Amodio, E. Yanac-Huertas, J. Ordoño, R. Rodriguez-Trujillo, J. Samitier, O. Castaño and E. Engel, *Biofabrication*, 2021, **13**, 035047.
30 Y. S. Zhang, A. Arneri, S. Bersini, S.-R. Shin, K. Zhu, Z. Goli-Malekabadi, J. Aleman, C. Colosi, F. Busignani, V. Dell'Erba, C. Bishop, T. Shupe, D. Demarchi, M. Moretti, M. Rasponi, M. R. Dokmeci, A. Atala and A. Khademhosseini, *Biomaterials*, 2016, **110**, 45–59.
31 G. C. Engelmayr, M. Cheng, C. J. Bettinger, J. T. Borenstein, R. Langer and L. E. Freed, *Nat. Mater.*, 2008, **7**, 1003–1010.
32 Y. J. Lee, Y. R. Kim, W. Y. Jeong, S. Lee, J. H. Shin and G.-J. Lee, *J. Nanosci. Nanotechnol.*, 2019, **19**, 6539–6545.
33 D. Kołodziejek, I. Łopianiak, O. Tadko, M. Drozd, M. Wojasiński and E. Jastrzębska, *Polym. Test.*, 2023, **127**, 108190.
34 M. S. Ahmed and H. A. Sadek, *JACC: Basic Transl. Sci.*, 2020, **5**, 461–462.
35 J. Veldhuizen, R. Chavan, B. Moghadas, J. G. Park, V. D. Kodibagkar, R. Q. Migrino and M. Nikkhah, *Biomaterials*, 2022, **281**, 121336.
36 G. Khanal, S. Hiemstra and D. Pappas, *Analyst*, 2014, **139**, 3274–3280.
37 S. Barmaki, V. Jokinen, D. Obermaier, D. Blokhina, M. Korhonen, R. H. A. Ras, J. Vuola, S. Franssila and E. Kankuri, *Acta Biomater.*, 2018, **73**, 167–179.
38 J. Park, S. Choo, S. M. Kim, T.-J. Jeon, Y. J. Heo and S. Kwon, *Microfluid. Nanofluid.*, 2022, **26**, 61.
39 A. Kobuszewska, E. Jastrzębska, K. Żukowski and Z. Brzózka, *Sci. Rep.*, 2020, **10**, 15524.
40 K. Tornberg, H. Välimäki, S. Valaskivi, A.-J. Mäki, M. Jokinen, J. Kreutzer and P. Kallio, *Biomed. Microdevices*, 2022, **24**, 34.
41 L. Zheng, B. Wang, Y. Sun, B. Dai, Y. Fu, Y. Zhang, Y. Wang, Z. Yang, Z. Sun, S. Zhuang and D. Zhang, *ACS Sens.*, 2021, **6**, 823–832.
42 M. L. Rexius-Hall, J. Rehman and D. T. Eddington, *Integr. Biol.*, 2017, **9**, 742–750.
43 K. Kopeć, M. Wojasiński and T. Ciach, *Int. J. Mol. Sci.*, 2020, **21**, 6798.
44 E. Liszewska, L. Majchrowicz, E. Krogulec, K. Kotulska, L. Kaczmarek, K. Kalita, A. Dobrzyń and J. Jaworski, *Stem Cell Res.*, 2021, **52**, 102225.
45 D. Kołodziejek, I. Łopianiak, O. Tadko, M. Drozd, M. Wojasiński and E. Jastrzębska, *Polym. Test.*, 2023, **127**, 108190.
46 D. Kołodziejek, U. Sierańska, Z. Iwoń, I. Łopianiak, E. Krogulec, M. Wojasiński and E. Jastrzębska, *Sens. Actuators, B*, 2024, **403**, 135169.
47 T. Kalogeris, C. P. Baines, M. Krenz and R. J. Korthuis, in *International Review of Cell and Molecular Biology*, Elsevier, 2012, vol. 298, pp. 229–317.
48 T. Tanaka, S. Tohyama, M. Murata, F. Nomura, T. Kaneko, H. Chen, F. Hattori, T. Egashira, T. Seki, Y. Ohno, U. Koshimizu, S. Yuasa, S. Ogawa, S. Yamanaka, K. Yasuda and K. Fukuda, *Biochem. Biophys. Res. Commun.*, 2009, **385**, 497–502.
49 R. Yu, U. Lendahl, M. Nistér and J. Zhao, *Front. Endocrinol.*, 2020, **11**, 374.
50 M. Sack, *Cardiovasc. Res.*, 2006, **72**, 210–219.
51 H. Zhu and H. F. Bunn, *Science*, 2001, **292**, 449–451.
52 S. Neubauer and N. Engl, *J. Med.*, 2007, **356**, 1140–1151.
53 E. Murphy and C. Steenbergen, *Physiol. Rev.*, 2008, **88**, 581–609.
54 F. Di Lisa, P. S. Blank, R. Colonna, G. Gambassi, H. S. Silverman, M. D. Stern and R. G. Hansford, *J. Physiol.*, 1995, **486**, 1–13.
55 G. Solaini, A. Baracca, G. Lenaz and G. Sgarbi, *Biochim. Biophys. Acta, Bioenerg.*, 2010, **1797**, 1171–1177.
56 D. M. Muntean, A. Sturza, M. D. Dănilă, C. Borza, O. M. Duicu and C. Mornoș, *Oxid. Med. Cell. Longevity*, 2016, **1**, 8254942.
57 L. J. Martin, *Pharmaceuticals*, 2010, **3**, 839–915.
58 J. M. Bliley, M. A. Stang, A. Behre and A. W. Feinberg, *Stem Cells Transl. Med.*, 2024, **13**, 425–435.
59 M. Carlos-Oliveira, F. Lozano-Juan, P. Occhetta, R. Visone and M. Rasponi, *Biophys. Rev.*, 2021, **13**, 717–727.
60 A. Vivas, C. IJspeert, J. Y. Pan, K. Vermeul, A. V. D. Berg, R. Passier, S. S. Keller and A. D. V. D. Meer, *Adv. Mater. Technol.*, 2022, **7**, 2101355.
61 Y. Liu, L. Lin and L. Qiao, *Anal. Bioanal. Chem.*, 2023, **415**, 3911–3925.

62 J.-L. Ruan, N. L. Tulloch, M. V. Razumova, M. Saiget, V. Muskheli, L. Pabon, H. Reinecke, M. Regnier and C. E. Murry, *Circulation*, 2016, **134**, 1557–1567.
63 G. Shi, C. Jiang, J. Wang, P. Cui and W. Shan, *Cell Tissue Res.*, 2024, **398**, 227–237.
64 G. J. Scuderi and J. Butcher, *Front. Cell Dev. Biol.*, 2017, **5**, 50.
65 J. Qin, A. Van Mil and J. P. G. Sluijter, in *Cardiac Mechanobiology in Physiology and Disease*, ed. M. Hecker and D. J. Duncker, Springer International Publishing, Cham, 2023, vol. 9, pp. 141–179.
66 G. J. Dugbartey, *Mol. Biol. Rep.*, 2024, **51**, 473.
67 E. E. Douzinas and A. Apeiranthitis, in *Modulation of Oxidative Stress in Heart Disease*, ed. S. Chakraborti, N. S. Dhalla, M. Dikshit and N. K. Ganguly, Springer Singapore, Singapore, 2019, pp. 645–670.
68 N. Chi, *Cardiovasc. Res.*, 2004, **61**, 437–447.
69 A. Gaitas, R. Malhotra, T. Li, T. Herron and J. Jalife, *Rev. Sci. Instrum.*, 2015, **86**, 034302.
70 F. Qian, C. Huang, Y.-D. Lin, A. N. Ivanovskaya, T. J. O'Hara, R. H. Booth, C. J. Creek, H. A. Enright, D. A. Soscia, A. M. Belle, R. Liao, F. C. Lightstone, K. S. Kulp and E. K. Wheeler, *Lab Chip*, 2017, **17**, 1732–1739.
71 A. Marsano, C. Conficconi, M. Lemme, P. Occhetta, E. Gaudiello, E. Votta, G. Cerino, A. Redaelli and M. Rasponi, *Lab Chip*, 2016, **16**, 599–610.
72 M. Gnecchi, Z. Zhang, A. Ni and V. J. Dzau, *Circ. Res.*, 2008, **103**, 1204–1219.
73 T. Sato and N. Takeda, *J. Cardiol.*, 2023, **81**, 202–208.
74 K. Wang, R. Ding, Y. Ha, Y. Jia, X. Liao, S. Wang, R. Li, Z. Shen, H. Xiong, J. Guo and W. Jie, *Acta Pharm. Sin. B*, 2018, **8**, 795–804.
75 W. Zhu, J. Chen, X. Cong, S. Hu and X. Chen, *Stem Cells*, 2006, **24**, 416–425.
76 C. Sid-Otmane, L. P. Perrault and H. Q. Ly, *J. Transl. Med.*, 2020, **18**, 336.
77 C. Xu, Y. Xie and B. Wang, *Stem Cell Res. Ther.*, 2024, **15**, 323.
78 P. Menasché, V. Vanneaux, A. Hagège, A. Bel, B. Cholley, A. Parouchev, I. Cacciapuoti, R. Al-Daccak, N. Benhamouda, H. Blons, O. Agbulut, L. Tosca, J.-H. Trouvin, J.-R. Fabreguettes, V. Bellamy, D. Charron, E. Tartour, G. Tachdjian, M. Desnos and J. Larghero, *J. Am. Coll. Cardiol.*, 2018, **71**, 429–438.
79 M. A. Laflamme, K. Y. Chen, A. V. Naumova, V. Muskheli, J. A. Fugate, S. K. Dupras, H. Reinecke, C. Xu, M. Hassanipour, S. Police, C. O'Sullivan, L. Collins, Y. Chen, E. Minami, E. A. Gill, S. Ueno, C. Yuan, J. Gold and C. E. Murry, *Nat. Biotechnol.*, 2007, **25**, 1015–1024.
80 E. Matsa, P. W. Burridge and J. C. Wu, *Sci. Transl. Med.*, 2014, **6**, 239.